

Effect of interactions on edge property measurements in magnetic multilayers

M. Zhu^{1,2} and R. D. McMichael¹

¹*Center for Nanoscale Science and Technology, National Institute of Standards and Technology, Gaithersburg, MD 20899, USA.*

²*Maryland Nanocenter, University of Maryland, College Park, MD 20742, USA*

(Dated: Sept 10, 2010)

This paper reports effects of inter-film interactions on static and dynamic magnetization behavior at film edges in magnetic trilayer stripe arrays under transverse applied fields. The trilayers consist of two magnetic films of $\text{Ni}_{80}\text{Fe}_{20}$, 10 nm and 20 nm thick that interact via dipolar fields across thin, nonmagnetic spacers from 1 nm to 20 nm thick. These trilayer films are patterned into stripe arrays by optical interference lithography. Ferromagnetic resonance spectra exhibit separate edge modes that are identified as excitation of edge modes primarily in one magnetic film or the other. When interlayer exchange is negligible, we observe several effects of dipolar edge-edge coupling including shifts of the edge saturation fields and changes in the mode intensity ratio relative to single-film edges. These interaction effects are reproduced by micromagnetic modeling and explained by simple models.

PACS numbers: 75.75.-c, 76.50.+g, 75.78.-n

I. INTRODUCTION

The material at the edges of lithographically patterned magnetic structures experiences processing conditions that are very different from the conditions away from the edge. In films that are patterned by ion milling, for example, the material at the film edge may be altered by the impact of the ions and by the redeposition of sputtered material. The material at the film edges, which is often unprotected by capping layers, is also vulnerable to oxidation¹. Because the qualities of the edges of patterned thin films are important in magnetic nanodevices such as magnetic random access memory (MRAM)², patterned hard drive media³, and other developing spin logic applications, we expect measurement of magnetic film-edge properties to become important for development of these new technologies.

One technique that has been developed to characterize the magnetic properties of thin film edges is edge mode ferromagnetic resonance (FMR) spectroscopy of transversely magnetized thin film stripes⁴. In this configuration, localized trapped spin wave modes or “edge modes” form in low-field regions near the stripe edges^{5,6}, and because these edge modes are localized within a few exchange lengths of the film edge, they are sensitive to the properties of the edge^{1,7,8}. Using the edge-mode FMR technique, the field required to saturate the magnetization perpendicular to the edges in arrays of $\text{Ni}_{80}\text{Fe}_{20}$ stripes can be measured with a precision of a few percent⁸.

To date, the edge mode FMR technique has been employed to study edges of only single-layer patterned films^{1,8-11}, but the need for edge property measurements in multilayer magnetic films is underscored by the development of devices based on giant magnetoresistance, tunneling magnetoresistance, and spin transfer torque where multilayers are used. In this work, we extend the edge mode FMR measurement technique to films with two magnetic layers, demonstrating the effects of interactions

between edge modes in the separate magnetic layers.

In section II, we present results of micromagnetic modeling that illustrate the effects of dipolar interactions between edge modes. In section III we describe sample preparation and measurement techniques and in section IV we compare the experimental results with the model predictions for static and dynamic interactions between the film edges.

II. MICROMAGNETIC SIMULATION

To guide interpretation of the experimental results presented below, we first discuss micromagnetic simulations¹² of a 500 nm wide stripe of 10 nm thick Py, 20 nm thick Py and a 10 nm Py / 2 nm spacer / 20 nm Py trilayer, with ideally smooth, vertical edges. We use the abbreviation “Py” to indicate a model material with properties similar to $\text{Ni}_{80}\text{Fe}_{20}$: saturation magnetization $M_s = 800$ kA/m, and exchange stiffness $A = 13$ pJ/m.

The static magnetization curve and equilibrium configuration of the trilayer are shown in Fig. 1. In zero applied field, the magnetization lies parallel to the y -axis due to shape anisotropy, along the length of the stripe. For increasing fields applied perpendicular to the stripe edges, along the x -axis, the magnetization rotates toward the x -direction, saturating at the center of the stripe first, and leaving edge curling walls at the edges¹¹. Fig. 1(b), inset (A) shows the edge curling walls with plots of the magnetization component along the stripe axis as a function of the distance from the edge. As the field is increased, the edge curling walls are eliminated one by one and the magnetization becomes nearly saturated perpendicular to the stripe edge, first in the thinner Py film, and then in the thicker Py film as shown in Fig. 1, insets (B) and (C).

The dynamic behavior of the trilayer stripe yields the resonances that we compare with experimental results to be described later. We simulate the resonant frequen-

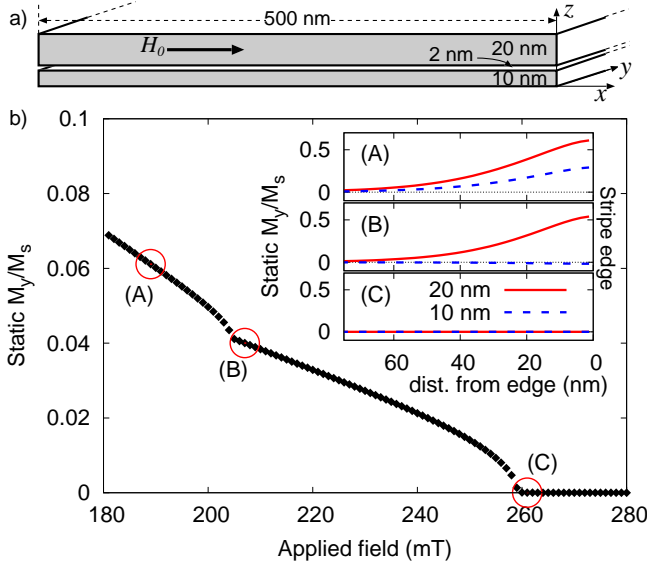


FIG. 1: Micromagnetic modeling of the transverse saturation of the edge magnetization in a 500 nm wide stripe of trilayer, 10 nm Py / 2 nm spacer / 20 nm Py. Panel (a) illustrates the stripe cross section. The magnetization component along the stripe axis is plotted in (b) as a function of the transverse applied field. For the labeled points, A, B and C, inset plots show profiles of the equilibrium magnetization near the film edges, showing that the edges saturate individually.

cies of the magnetization using a ground, pulse, ring and Fourier transform method^{13,14}. Fig. 2(a) shows the simulated resonance frequencies for separate stripes of 20 nm and 10 nm Py thicknesses over a range of applied fields. The areas of the circular symbols are proportional to the mode intensities in a uniform driving field. Restricting attention to fields above 0.25 T, these spectra can be divided into a group of bulk modes appearing at higher frequencies (or lower fields) and localized edge modes appearing at lower frequencies (or higher fields)⁵⁻⁷. Following the edge mode of the thicker film in decreasing applied fields, the edge mode frequency approaches zero at an applied field of ≈ 0.22 T. At this field, the edge magnetization in the thicker film is neutrally stable. For higher fields, the edge magnetization is aligned perpendicular to the edge, and at lower fields, the magnetization in the thicker film forms an edge curling wall with an amount of curling that depends on the applied field as shown in Fig. 1. Similarly, the edge saturation field of the 10 nm film is 0.15 T.

The mode frequencies for the combined 10 nm Py / 2 nm spacer / 20 nm Py trilayer stripe are shown in Fig. 2(b). By comparison with the spectra of the single-layer stripes one can identify bulk modes and edge modes, and edge saturation fields of the individual films are identifiable at the fields where the edge mode frequencies go to zero. With one caveat, we find that both simulated and measured edge mode frequencies fit well to a modi-

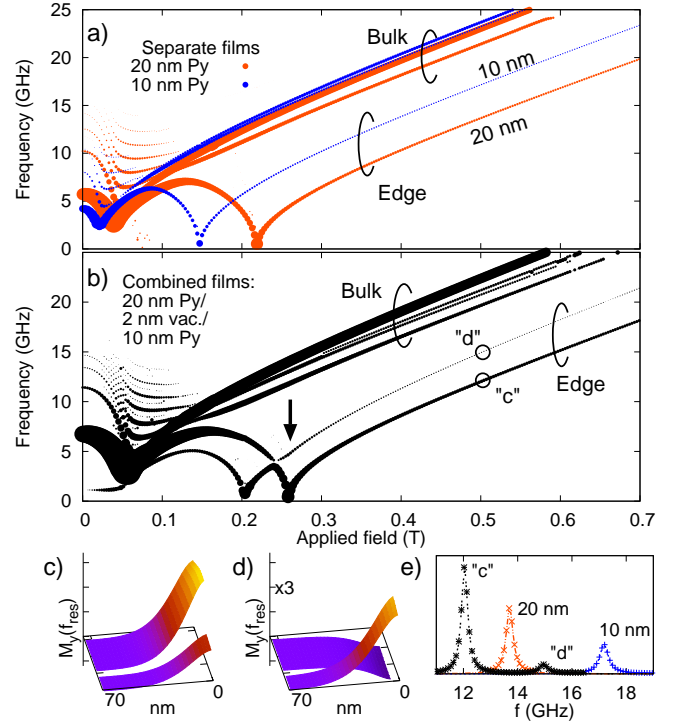


FIG. 2: (a) Ferromagnetic resonance frequencies calculated separately for 500 nm wide stripes of Py for fields applied transverse to the stripe axes. The sharp, zero-frequency minima correspond to saturation of the magnetization at the edges. (b) Ferromagnetic resonance frequencies calculated for a 500 nm wide stripe of trilayer, 10 nm Py / 2 nm spacer / 20 nm Py as a function of applied field. Low frequency cusps occur at the edge saturation fields. At high fields, the two lower resonance frequencies are associated with edge modes that involve precession mainly in one film or the other, as shown in (c) and (d). Changes in the mode intensity (e) result from in-phase (c) or out-of-phase (d) precession of the weakly excited edge mode.

fied Kittel formula^{7,15},

$$f_i = \gamma_f \mu_0 [(H_0 - H_{\text{sat},i})(H_0 + H_{2,i})]^{1/2}. \quad (1)$$

where $\gamma_f = 29.3$ GHz/T, $\mu_0 = 4\pi \times 10^{-7}$ N/A² is the permeability of vacuum, H_0 is the applied field, and fit parameters $H_{\text{sat},i}$ and $H_{2,i}$ are the effective edge saturation field and the effective out-of-plane anisotropy⁷, respectively for the edge mode of each layer (i).

Differences between a superposition of the single-film resonances in Fig. 2(a) and the resonances of the combined structure in Fig. 2(b) reveal the influence of interactions between the films, which are entirely due to magnetostatic effects in this model. The most visible interaction effect is an upward shift of both the edge saturation fields from their single-film values. The H_{sat} values and their dependence on the nonmagnetic spacer layer thickness will be discussed together with the experimental results in Section IV.

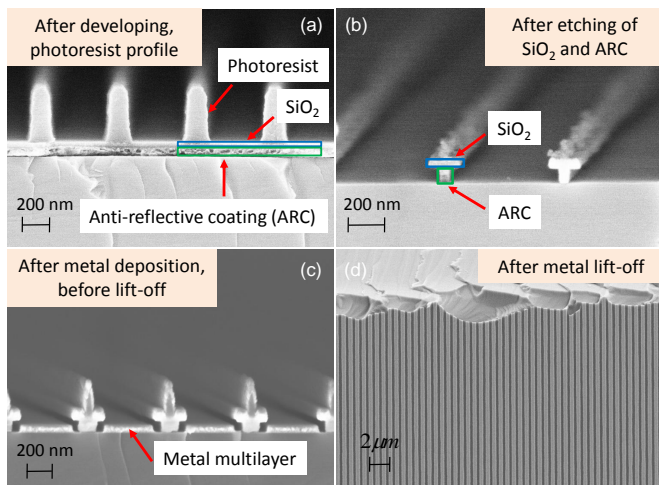


FIG. 3: Scanning Electron Microscope (SEM) images at different fabrication steps. (a-c) cross sections and (d) stripe array near a cleaved edge (top view).

A subtler indication of the interactions is a kink (see arrow in Fig. 2(b) in the frequency of the 10 nm film edge mode at the field where the frequency of the 20 nm film edge mode goes to zero, and the ground state of the 20 nm film changes from saturated to an edge curling wall. The presence of the kink leads to a distinction between the effective value of H_{sat} obtained from a fit to Eq. (1) and the actual saturation field for the thin film, where the edge mode frequency approaches zero. This is the caveat mentioned above. For fitting of both the model results and the measured results we only consider the data for fields above the saturation fields. From a theoretical standpoint, this high field region is the less complicated region, because equilibrium states are nearly independent of applied field.

A third indication of the interactions is a change in the relative intensities of the two edge modes. The spatial profiles of the edge modes at the resonance frequencies marked in Fig. 2(b) are shown in Fig. 2(c) and (d). These profiles of the imaginary component of the magnetization at the resonance frequencies reveal that while precession in these modes is associated predominantly with one film or the other, coupling does cause the weakly excited edge to precess either in phase (c) or out of phase (d) with the strongly excited edge, resulting in either an enhanced or diminished mode intensity as shown in Fig. 2(e).

In the rest of the paper we focus on the changes in H_{sat} and changes in mode intensity as metrics of edge interactions.

III. EXPERIMENTAL

The samples are arrays of long parallel multilayer stripes, approximately 380 nm wide with a 610 nm pitch fabricated by optical interference lithography, electron

beam evaporation and lift-off with an undercut mask¹⁶. Fig. 3 shows the fabrication steps. A trilayer stack comprised of 90 nm antireflective coating (ARC), 30 nm SiO₂ and 400 nm of photoresist was subsequently spun on or sputtered on a Si substrate. The photoresist was exposed in a Lloyd's mirror interference lithography configuration¹⁷ with a laser diode at a wavelength of 405 nm, and then developed to form a grating pattern in the resist [Fig. 3(a)]. The stripe pattern was then transferred to the underlying SiO₂ by reactive ion etching and an oxygen plasma was used to partially remove the ARC layer to form a T-shaped mask for metal lift-off [Fig. 3(b)]. Metal multilayer films were evaporated on this mask template [Fig. 3(c)] and finally metal stripes were obtained by lifting-off the ARC in a photoresist developer [Fig. 3(d)].

The multilayer metal films have the structure: Si / SiO_x / 3 nm Ta / 10 nm Ni₈₀Fe₂₀ / x Cu / 20 nm Ni₈₀Fe₂₀ / 10 nm Cu cap, where the Cu spacer thickness, x , ranges from 1 nm to 20 nm. Also, two single-layer stripe arrays with the structure: 3 nm Ta / t Ni₈₀Fe₂₀ / 10 nm Cu cap were fabricated for t of 10 nm and 20 nm as control samples without interlayer interactions. All the samples were fabricated from the pieces cut from a single T-shaped mask template to minimize the variation in stripe dimensions.

FMR measurements were made with samples placed face down on a coplanar waveguide with the stripes aligned perpendicular to a slowly varying applied field H_0 to within $\pm 0.1^\circ$. FMR spectra were obtained by monitoring the signal transmitted through the coplanar waveguide, with isolation of magnetic resonances achieved by applying a weak (< 0.5 mT amplitude) oscillating field in parallel with H_0 , and demodulating the detected microwave power with a lockin amplifier⁸. FMR spectra were taken at frequencies ranging from 0.1 GHz to 25 GHz.

IV. RESULTS

Fig. 4 shows the field-frequency map for the observed modes in the multilayer stripes with a 2 nm spacer. Clearly visible in the map are two low-frequency, high-field modes that we identify as the edge modes of the two Ni₈₀Fe₂₀ films. One clear difference between the measured and modeled resonances is that the measured edge resonances occur at lower field than the model edge resonances. Similar differences have been observed in studies of single-layer edges^{4,9}, and we attribute them to non-ideality of the experimental sample edges arising from a number of possible mechanisms including non-vertical side walls¹¹, dilution of the magnetization near the edge¹ and surface anisotropy on the edge surface⁷. Another clear difference between the measured and modeled results is the absence of visible edge mode resonances in the measured spectra just below the edge saturation field. The model predicts strong resonances that approach zero

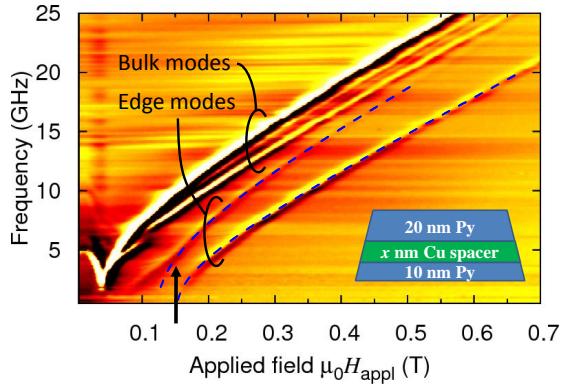


FIG. 4: Field dependence of ferromagnetic resonance frequencies in a 10 nm $\text{Ni}_{80}\text{Fe}_{20}$ / 2 nm Cu / 20 nm $\text{Ni}_{80}\text{Fe}_{20}$ trilayer. The higher intensity, higher frequency modes are bulk modes and the weaker, lower frequency modes are edge modes. Dashed lines are fits described in the text.

frequency as the field approaches edge saturation fields from below. The origins of this difference are not clear, but the absence of these resonances is not unique to the multilayer edges. In single layer edges, the resonances are observed only weakly, and only in some samples^{1,8}.

As predicted by the simulations, a subtle kink is visible in the higher frequency (thinner film) edge mode frequency at the field where the lower frequency (thicker film) mode extrapolates to zero frequency. (See arrow in Fig. 4.) This kink was the strongest for 2 nm Cu spacer sample, becoming weaker with increasing Cu spacer thickness, but remaining visible up to $x = 15$ nm.

At 1 nm spacer thickness we observe only one edge mode across all the frequencies, and we speculate that strong exchange coupling may have developed across this thin spacer, causing the two films to precess in unison.

A. Static dipolar interactions

We quantify the field dependence of the edge mode frequencies by fitting to Eq. (1). The effective edge saturation field, H_{sat} , and H_2 , an effective out-of-plane anisotropy, are treated as fit variables and the gyromagnetic ratio γ_f is held fixed at 29.3 GHz/T. Example fits are shown in Fig. 5. For these fits, we use only data from fields greater than the kink field, where both edges are saturated.

Fig. 6 shows plots of effective edge saturation fields as a function of inverse center-to-center film separation, $1/(t_{\text{Cu}} + 15 \text{ nm})$. Moving from left to right in this plot we move from independent, single films on the left to highly interacting films with a decreasing spacer to the right. The upper set of diamond symbols are the edge saturation fields of micromagnetic simulations with varying spacer thickness. The lower circular symbols are the measured edge saturation fields for samples with the cor-

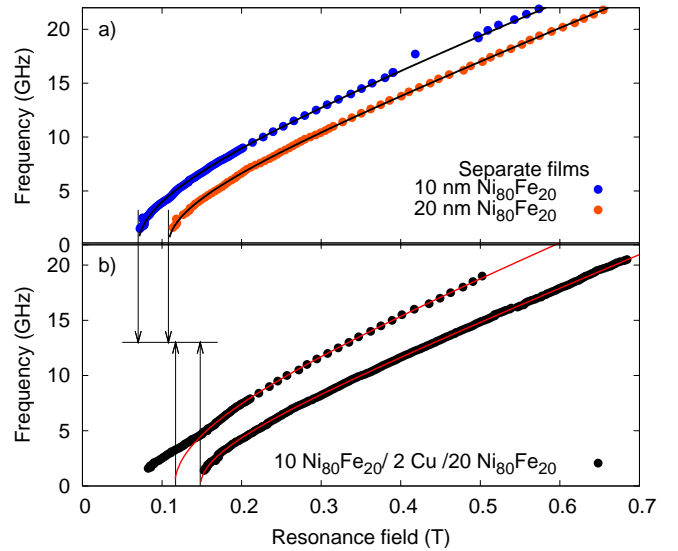


FIG. 5: (Color online) Applied field dependence of edge mode frequencies in 10 nm and 20 nm thick stripe arrays, measured a) separately, and b) together in 10 nm $\text{Ni}_{80}\text{Fe}_{20}$ / 2 nm Cu / 20 nm $\text{Ni}_{80}\text{Fe}_{20}$ stripes. The solid lines are fits to the data. In b), the fit of the higher frequency resonance is restricted to fields above the kink.

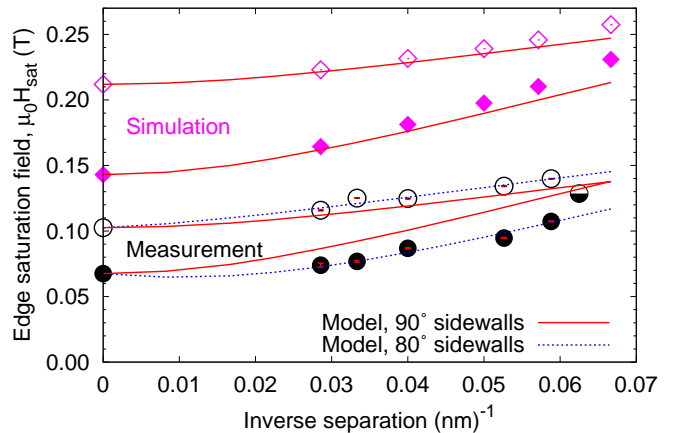


FIG. 6: Effective edge saturation fields as a function of the inverse center-to-center separation of two $\text{Ni}_{80}\text{Fe}_{20}$ films. The diamond symbols are micromagnetic simulation results and the circular symbols are from fits to the measurements. Open and filled symbols are for 20 nm and 10 nm edge resonances, respectively. The half-filled symbol is from the single edge mode resonance of the sample with a 1 nm spacer layer. Lines are the predictions of a simplified model of static dipolar interactions that is described in the text.

responding spacer thicknesses. The standard deviations of the fits are indicated by error bars, and are generally smaller than the symbol size. We attribute the scatter of the data to variations arising in sample preparation. For both sets of data, open symbols correspond to the lower frequency (mostly thick film) edge resonance and filled

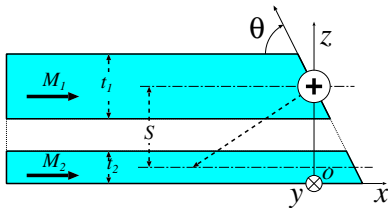


FIG. 7: Geometry of a simple model describing magnetostatic interactions between saturated films.

symbols correspond to the higher frequency (mostly thin film) edge resonance.

The local effective applied field near any stripe edge includes stray fields from magnetostatic charge at other edges in the sample, and the magnitudes of these stray fields depend on whether the sample is a single stripe or an array, the stripe or array dimensions, and on the total magnetic thickness of the sample. The values of H_{sat} plotted in Fig. 6 have been corrected for these stray fields to yield values of H_{sat} that correspond to the local applied field. These corrections are less than 10 mT in all cases.

The solid and dotted lines in Fig. 6 are the predictions of a simplified edge mode interaction model that uses the geometry illustrated in Fig. 7. The mid-planes of the two films are separated by a distance s and the magnetization is assumed saturated in the $+x$ direction. For simplicity, we approximate the magnetostatic charge distributed on the edge of the top film with a line charge, and the x -component of the field at the mid-plane of the bottom film can be written,

$$H_{x,2}(s, x) \approx \frac{M_1 t_1}{2\pi} \frac{x}{(x^2 + s^2)}. \quad (2)$$

This static field in the bottom film affects the edge mode resonance only to the extent that it is significant in the region where the edge mode precession is large. We determine the effective edge mode interaction field by weighting the static field by the square^{18,19} of the edge mode precession amplitudes, $m_y(x)$, shown in Fig. 2(c) and (d).

$$H_{xx,2}^{\text{int}}(s) = \frac{\int_{-\infty}^{s \cot \theta} H_{x,2}(s, x) [m_{y,1}(x - s \cot \theta)]^2 dx}{\int_{-\infty}^0 [m_{y,1}(x)]^2 dx}. \quad (3)$$

To calculate the effective interaction field on the upper film, one can use Eqs. (2) and (3) substituting M_2 and t_2 for M_1 and t_1 , respectively, and substituting $(\pi - \theta)$ for θ .

With the geometry of Fig. 7, it is clear that H_x and H_{int} are negative for $\theta = \pi/2$, i.e. the effective field at an edge is reduced by the interaction. It follows that this interaction will increase the applied field needed to saturate the edge or to achieve resonance at a given frequency. We plot $H_{\text{sat}}(s \rightarrow \infty) - H_{xx}^{\text{int}}(s)$ as a function of inverse separation $1/s$ in Fig. 6 as solid lines when assuming vertical side walls on the stripe edges ($\theta = \pi/2$).

We use $H_{\text{sat}}(s \rightarrow \infty) = 0.22$ T and 0.15 T for the modeled lines to compare with the micromagnetic simulation and use $H_{\text{sat}}(s \rightarrow \infty) = 0.11$ T and 0.07 T for the modeled lines to compare with the measured results. The agreement of this simple model with the micromagnetic model is good, except where the spacer layer becomes thin, where the static field model underestimates the effects of interaction. We speculate that this is because the line charge approximation of the magnetostatic charges at the edge loses validity for films in close proximity.

The significant differences between the modeled, ideal edge saturation field values and the measured values make clear that the measured edges are not ideal. Modeling has shown that tilting of the side walls, dilution of the edge magnetization and surface anisotropy associated with symmetry breaking at the edge surfaces can all reduce H_{sat} relative to the ideal edge value⁷. Further, measurements have confirmed the effects of sidewall angle⁸, and oxidation of stripe edges also reduces H_{sat} ¹.

The static field model applied to the measured values produces the lower set of solid lines, where the agreement with the spacer thickness dependence is less satisfactory. Recognizing the nonideality of the stripe edges, we plot the static field model with a side wall angle $\theta = 80^\circ$ (dotted lines in Fig. 6), which gives a better agreement with the measured dependence on the spacer thickness.

We note that the model predicts tilting the side walls by 10° has a larger effect on the thin film (lower H_{sat}) than on the thicker film. When the side wall is tilted, as shown in Fig. 7, the x -component of the field due to the charge on the edge of the upper film takes on both positive and negative values in the lower film and in (3). In contrast, the interaction field acting on the upper film is reduced, but remains negative for all x .

B. Dynamic dipolar interactions

The static interaction fields described in the previous subsection, IV A, account for changes in the effective edge saturation fields of the two edge mode resonances. However, the coupled precession that is evident in Figs. 2(c)-(d) and the peak intensities of Fig. 2(e) indicates that dynamic interactions as well as static interactions are important features of the localized precession at the film edges. In this subsection, we describe the effects of dynamic interactions on the mode intensities, using a model of two interacting macrospins to guide interpretation of the experimental results.

Fig. 8(a) shows the simulated and measured dependence of the resonance intensity ratio I_c/I_d on the center-to-center spacing of the magnetic films, where the subscript c and d correspond to the edge modes shown in Fig. 2(b). As we will show below, the interactions that are responsible for these intensity effects are the z -components of dipolar fields due to the oscillating z -components of the magnetization in the edge mode precession.

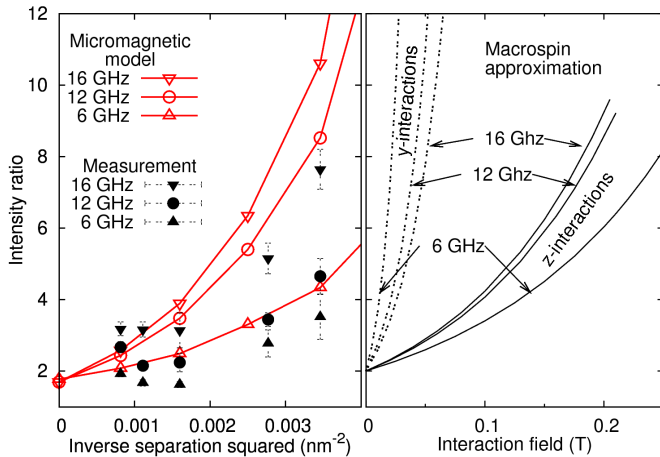


FIG. 8: Ratio of the higher-field to lower-field edge mode resonances obtained from measurements and micromagnetic modeling (left panel) and from a two-macrospin model (right panel).

The measured mode intensities were calculated from the individual spectra that comprise Fig. 4. These spectra were recorded as a function of the slowly swept applied field using field modulation and a lockin amplifier, and the spectra approximate field derivatives of Lorentzian absorption peaks. The experimental intensity ratios were obtained by fitting the spectra to the derivatives of Lorentzians and then using the fit parameters to compute the field-integrated intensities. Error bars representing one standard deviation are derived from the uncertainties in the Lorentzian fit.

In contrast, the simulated spectra are obtained from the Fourier transform of a time series, and the resonances emerge as a function of frequency, not field. We therefore approximate the field-integrated intensities as

$$I \propto \int \chi''(H, f) dH \approx \frac{dH}{df} \int \chi''(H, f) df, \quad (4)$$

where we use Eq.(1) to evaluate dH/df , the slope of the resonance frequency vs. field plot.

We plot the measured and modeled intensity ratios in Fig. 8. The dynamic interaction fields will arise from oscillating dipoles, and we anticipate that at large separations (at least within the near field), these dynamic fields will decay asymptotically as $1/s^2$ like the field due to a dipole line charge. For this reason, we plot the intensity ratio as a function of the square of the inverse separation $1/s^2$. Two common trends in the measured and modeled data are apparent: the intensity ratios become larger as the film separation decreases as expected for increasing interaction, but they also become larger for spectra that are measured/simulated at higher frequencies.

To guide interpretation of these results, we use a coupled macrospin model where we consider only the magnetization near the edge of the sample, and we represent edge mode precession in the individual films as sin-

gle precessing macrospins. This approximation has been used previously to describe edge mode dynamics in single films⁷, and here it makes it convenient to include and manipulate interactions explicitly, and it allows us to estimate the magnitude of interaction fields. Details of the interacting macrospin model are presented in the appendix. The interaction field acting on macrospin in film i due to the magnetization of macrospin in film j is written as

$$\mathbf{H}_i^{\text{int}} = H_{xx}^{\text{int}}(s)\hat{\mathbf{x}} + H_{yy,i}^{\sigma}(s)\frac{M_{y,j}}{M_{s,j}}\hat{\mathbf{y}} + H_{zz,i}^{\sigma}(s)\frac{M_{z,j}}{M_{s,j}}\hat{\mathbf{z}}. \quad (5)$$

The first term in this expression is the static x -component of the interaction field, discussed in the preceding section, which adds to the applied field and shifts the resonances and H_{sat} values as shown in Fig. 6. The last two terms are dynamic interaction fields with parameters $H_{yy,i}^{\sigma}(s)$ and $H_{zz,i}^{\sigma}(s)$, which describe the maximum interaction fields. To use the z -component as an example, $H_{zz,i}^{\sigma}(s)$ is the maximum z -component of the interaction field, which is obtained when the magnetization of the “source” film is saturated in the z -direction.

The dynamic interaction fields are responsible for changes in the relative intensities of the edge modes. When the lower-frequency mode is driven near its resonance, the interaction fields excite the higher frequency mode below its resonance where its response will be in phase with the interaction field, and therefore in-phase with the low-frequency mode response, adding to the intensity. Conversely, if the higher frequency mode is driven near its resonance, the lower-frequency mode will be excited above its resonance frequency and the low-frequency mode’s response will be out of phase, reducing the mode intensity.

Fig. 8(b) shows the integrated intensity ratio obtained from the coupled macrospin model. Two sets of curves are shown, one for interactions solely between the z -components of the macrospins, and the other for interactions solely between the y -components of the macrospins. Unlike the micromagnetic model and the experimental data, y -interactions cause the intensity ratio to decrease with frequency. In contrast, the z -interactions produce intensity ratios that increase with frequency, reproducing the trends shown in Fig. 8(a).

For these calculations the x -interaction fields have been held constant to isolate effects of only the dynamic interaction fields on the resonance fields and intensities. The dynamic interactions have a large effect on the mode intensity ratio, which initially increases linearly and grows by a factor of 6 over the shown range of interaction field.

In the macrospin model, dynamic interaction field parameters on the order of 0.1 T are required to produce intensity ratios in the macrospin model that are comparable to those observed in the experiment and micromagnetic modeling. To show that these values are reasonable, recall that the interaction field parameter is defined in terms of saturated magnetization in the “source” macrospin. If the macrospin in the thicker film is re-

garded as a dipole line charge in the z direction, the field at the center of the thinner film can be approximated as

$$H_{zz}^{\text{int}} \approx \frac{M_{s,j}(\pi t_j d_e/4)}{2\pi s^2}. \quad (6)$$

For a 5 nm spacer layer thickness ($s = 20$ nm) and an edge mode depth, $d_e \approx 27$ nm⁷, $\mu_0 H_{zz}^{\text{int}} \approx 0.17$ T, which corresponds nicely to the interaction field scale of Fig. 8(b). We stress here that while H_{zz}^{int} is a large field, it is only a parameter that describes the interaction. Actual fields encountered during precession are smaller by a factor of $M_z/M_s \ll 1$ as shown in Eq. (5).

V. CONCLUSION

In this paper, we have demonstrated an extension of edge mode spectroscopy to stripe arrays of multilayers with two dissimilar magnetic layers. In increasing magnetic fields oriented perpendicular to the edges, modeling shows that saturation of the edge magnetization occurs separately for each film when exchange interactions are negligible. At higher fields, we measure two edge modes with extrapolated edge saturation fields that are modestly larger than the corresponding single-film values, and we explain these field shifts as a static dipolar interaction. Also, as the spacer layer becomes thinner, the intensity of the lower-frequency edge mode becomes relatively larger than the higher frequency mode. The intensity ratio changes are explained by interaction fields along the film normal, and they are more sensitive to the interactions than the resonance field shift.

The authors acknowledge the support of the Maryland Nanocenter and assistance from the staff of the NIST NanoFab.

Appendix: Interacting macrospin model

We write the edge mode macrospin magnetizations $\mathbf{M}_i(t)$ in terms of a static component $M_{s,i}$ saturated in the $\hat{\mathbf{x}}$ direction and a small dynamic component $\mathbf{m}_i(t)$ in the y - z plane. The Landau-Lifshitz-Gilbert equations of motion are

$$\frac{d\mathbf{m}_i}{dt} = -\mu_0|\gamma|(\mathbf{M}_i \times \mathbf{H}_i^{\text{eff}}) + \frac{\alpha}{M_{s,i}} \left(\mathbf{M}_i \times \frac{d\mathbf{m}_i}{dt} \right), \quad (\text{A.1})$$

where $\mu_0 = 4\pi \times 10^{-7}$ T m/A is the permeability of free space, $\gamma \approx 2.21 \times 10^5$ m/As and $\alpha \approx 0.007$ is a typical Gilbert damping parameter for Ni₈₀Fe₂₀.

The effective field $\mathbf{H}_i^{\text{eff}}$ includes the applied field, exchange field and dipolar fields that act on the macrospins. Below we discuss separately two components of $\mathbf{H}_i^{\text{eff}}$: the fields that act on non-interacting edge modes $\mathbf{H}_i^{\text{iso}}$, and the interaction fields $\mathbf{H}_i^{\text{int}}$.

For non-interacting film edges, the fields acting on the edge macrospins are summarized by

$$\begin{aligned} \mathbf{H}_i^{\text{iso}} &= (H_0 - H_{\text{sat},i})\hat{\mathbf{x}} - N_{z,i}m_{z,i}\hat{\mathbf{z}} \\ &+ H_{\text{pump}}e^{i\omega t}\hat{\mathbf{y}}, \end{aligned} \quad (\text{A.2})$$

where $H_{\text{sat},i}$, which includes exchange interactions⁷, acts as a demagnetizing field in the x direction, $-N_{z,i}m_{z,i}\hat{\mathbf{z}}$ is an effective demagnetization field in the z -direction, and H_{pump} is a microwave-frequency excitation field. Substituting $\mathbf{H}_i^{\text{iso}}$ for $\mathbf{H}_{i,\text{eff}}$ in Eq. (A.1), and defining $H_{2,i} \equiv N_{z,i}M_{s,i} - H_{\text{sat},i}$ these fields yield equation (1) for each isolated film edge.

The interaction energy of edge macrospins can be expressed generally as

$$E_{\text{int}} = \mathbf{M}_{\text{top}} \cdot \boldsymbol{\sigma} \cdot \mathbf{M}_{\text{bottom}}, \quad (\text{A.3})$$

where $\boldsymbol{\sigma}$ is a tensor that we will assume to be diagonal, and interaction fields are parameterized by

$$\mathbf{H}_{aa,i}^{\sigma} = \frac{\sigma_{aa} \cdot M_{s,j}\hat{\mathbf{a}}}{\mu_0 v_i}, \quad i \neq j. \quad (\text{A.4})$$

where v_i is the volume of the region represented by the macrospin and $\hat{\mathbf{a}}$ is a unit vector in the a -direction. As in ref. 7 we assume that the volume v_i represented by the macrospin in film i is an ellipsoidal cylinder at the film edge bounded by the film thickness t_i , the depth that the edge mode extends into the film $d_{e,i} \approx 27$ nm, and the length of the stripe, L .

Several authors have addressed the dynamics of extended magnetic films coupled by isotropic exchange interactions where $\sigma_{xx} = \sigma_{yy} = \sigma_{zz} = -J$, and the energy of interaction can be written as $-JM_i \cdot M_j$ ²⁰⁻²⁴. For the edge mode macrospins interacting via dipolar interactions, the interaction tensor is anisotropic, $\sigma_{xx} \neq \sigma_{yy} \neq \sigma_{zz}$.

The static x interaction fields, $H_{xx,i}^{\text{int}}$ were estimated explicitly as a function of film separation s in section IV A. We expect that the y -interaction fields $\mathbf{H}_{yy,i}^{\sigma}$ will be small since y -components of the magnetization do not generate any stray field for smooth, straight edges. However we do allow for the possibility of y interactions in the following analysis. Finally, $\mathbf{H}_{zz,i}^{\sigma}$ describes the stray fields due to the dynamic z -component of the magnetization.

The interaction field given by (5) is repeated here for clarity.

$$\mathbf{H}_i^{\text{int}} = H_{xx}^{\text{int}}(s)\hat{\mathbf{x}} + H_{yy,i}^{\sigma}(s)\frac{m_{y,j}}{M_{s,j}}\hat{\mathbf{y}} + H_{zz,i}^{\sigma}(s)\frac{m_{z,j}}{M_{s,j}}\hat{\mathbf{z}}. \quad (\text{A.5})$$

Summing the interaction fields in (A.5) with the fields acting on isolated edges (A.2), one can see that the static $H_{xx}^{\text{int}}(s)$ adds to the applied field and shifts the edge mode resonances. When substituted into (A.1), the effective field given by $\mathbf{H}_i^{\text{eff}} = \mathbf{H}_i^{\text{iso}} + \mathbf{H}_i^{\text{int}}$ leads to a system of four coupled equations of motion for the y - and z -components of the two macrospins. We solve these equations numerically to obtain the susceptibility, $\chi_{yy}(H_0, \omega)$.

$$\chi_{yy}(H_0, \omega)H_{\text{pump}} = \mathbf{m}_{1,y}(\omega) + \mathbf{m}_{2,y}(\omega). \quad (\text{A.6})$$

For each frequency, the imaginary component of $\chi_{yy}(H_0)$ exhibits two peaks as a function of field, and we fit these peaks to a pair of Lorentzians to obtain the intensity ratio

and resonance field shifts generated by the macrospin model.

-
- ¹ M. Zhu and R. D. McMichael, *J. Appl. Phys.* **107**, 103908 (2010).
- ² M. Yoshikawa, E. Kitagawa, S. Takahashi, T. Kai, M. Amano, N. Shimomura, T. Kishi, S. Ikegawa, Y. Asao, H. Yoda, et al., *J. Appl. Phys.* **99**, 08R702 (2006).
- ³ J. M. Shaw, S. E. Russek, T. Thomson, M. J. Donahue, B. D. Terris, O. Hellwig, E. Dobisz, and M. L. Schneider, *Phys. Rev. B* **78**, 024414 (2008).
- ⁴ B. B. Maranville, R. D. McMichael, S. A. Kim, W. L. Johnson, C. A. Ross, and J. Y. Cheng, *J. Appl. Phys.* **99**, 08C703 (2006).
- ⁵ J. Jorzick, S. O. Demokritov, B. Hillebrands, M. Bailleul, C. Fermon, K. Y. Guslienko, A. N. Slavin, D. V. Berkov, and N. L. Gorn, *Phys. Rev. Lett.* **88**, 047204 (2002).
- ⁶ J. P. Park, P. Eames, D. M. Engebretson, J. Berezovsky, and P. A. Crowell, *Phys. Rev. Lett.* **89**, 277201 (2002).
- ⁷ R. D. McMichael and B. B. Maranville, *Phys. Rev. B* **74**, 024424 (2006).
- ⁸ B. B. Maranville, R. D. McMichael, and D. W. Abraham, *Appl. Phys. Lett.* **90**, 232504 (2007).
- ⁹ R. D. McMichael, C. A. Ross, and V. P. Chuang, *J. Appl. Phys.* **103**, 07C505 (2008).
- ¹⁰ M. Bailleul, D. Olligs, C. Fermon, and S. O. Demokritov, *Europhys. Lett.* **56**, 741 (2001).
- ¹¹ M. Bailleul, D. Olligs, and C. Fermon, *Phys. Rev. Lett.* **91**, 137204 (2003).
- ¹² M. J. Donahue and D. G. Porter, in *Interagency Report NISTIR 6376* (National Institute of Standards and Technology, Gaithersburg, MD, 1999).
- ¹³ O. Gérardin, H. Le Gall, M. J. Donahue, and N. Vukadinovic, *J. Appl. Phys.* **89**, 7012 (2001).
- ¹⁴ R. D. McMichael and M. D. Stiles, *J. Appl. Phys.* **97**, 10J901 (2005).
- ¹⁵ C. Kittel, *Phys. Rev.* **73**, 155 (1948).
- ¹⁶ J. Y. Cheng, C. A. Ross, E. L. Thomas, H. I. Smith, and G. J. Vansco, *Appl. Phys. Lett.* **81**, 3657 (2002).
- ¹⁷ M. E. Walsh, Ph.D. thesis, Massachusetts Institute of Technology (2004).
- ¹⁸ K. Y. Guslienko, R. W. Chantrell, and A. N. Slavin, *Phys. Rev. B* **68**, 024422 (2003).
- ¹⁹ Y. Obukhov, D. V. Pelekhov, J. Kim, P. Banerjee, I. Martin, E. Nazaretski, R. Movshovich, S. An, T. J. Gramila, S. Batra, et al., *Phys. Rev. Lett.* **100**, 197601 (2008).
- ²⁰ B. Heinrich, S. T. Purcell, J. R. Dutcher, K. B. Urquhart, J. F. Cochran, and A. S. Arrott, *Phys. Rev. B* **38**, 12879 (1988).
- ²¹ J. J. Krebs, P. Lubitz, A. Chaiken, and G. A. Prinz, *J. Appl. Phys.* **67**, 5920 (1990).
- ²² A. Layadi and J. O. Artman, *J. Magn. Magn. Mater* **92**, 143 (1990).
- ²³ Z. Zhang, L. Zhou, P. E. Wigen, and K. Ounadjela, *Phys. Rev. B* **50**, 6094 (1994).
- ²⁴ S. M. Rezende, C. Chesman, M. A. Lucena, A. Azevedo, F. M. de Aguiar, and S. S. P. Parkin, *J. Appl. Phys.* **84**, 958 (1998).